

# Jahn-Teller distortion around $\text{Fe}^{4+}$ in $\text{Sr}(\text{Fe}_x\text{Ti}_{1-x})\text{O}_{3-\delta}$ from x-ray absorption spectroscopy, x-ray diffraction, and vibrational spectroscopy

M. Vračar,<sup>1</sup> A. Kuzmin,<sup>2</sup> R. Merkle,<sup>1,\*</sup> J. Purans,<sup>2</sup> E. A. Kotomin,<sup>1</sup> J. Maier,<sup>1</sup> and O. Mathon<sup>3</sup>

<sup>1</sup>Max-Planck-Institut für Festkörperforschung, Heisenbergstrasse 1, Stuttgart D-70569, Germany

<sup>2</sup>Institute of Solid State Physics, University of Latvia, Kengaraga Street 8, LV-1063 Riga, Latvia

<sup>3</sup>European Synchrotron Radiation Facility, BP 220, 38043 Grenoble, France

(Received 12 December 2006; revised manuscript received 3 September 2007; published 12 November 2007)

$\text{Sr}(\text{Fe}_x\text{Ti}_{1-x})\text{O}_{3-\delta}$  perovskites (strontium titanate ferrite solid solution) with well-defined oxygen stoichiometry have been studied as a function of iron concentration by x-ray diffraction, Fe and Ti  $K$ -edge x-ray absorption spectroscopy (XAS), and vibrational (Raman and infrared) spectroscopy. In reduced  $\text{Sr}(\text{Fe}_x\text{Ti}_{1-x})\text{O}_{3-x/2}$  samples, the analysis of the Fe  $K$ -edge extended x-ray absorption fine structure indicates the expected presence of oxygen vacancies  $V_{\text{O}}^{\bullet}$  in the first coordination shell of  $\text{Fe}^{3+}$  ions. In oxidized  $\text{Sr}(\text{Fe}_x\text{Ti}_{1-x})\text{O}_3$  samples, the combination of XAS and vibrational spectroscopy results yields strong indications for the presence of a Jahn-Teller distortion around  $\text{Fe}^{4+}$  ions, which is most pronounced for  $x \approx 0.03$  and decreases for higher iron concentrations.

DOI: 10.1103/PhysRevB.76.174107

PACS number(s): 61.10.Ht, 78.70.Dm, 61.10.Nz, 78.30.-j

## I. INTRODUCTION

The perovskite solid solution series  $\text{Sr}(\text{Fe}_x\text{Ti}_{1-x})\text{O}_{3-\delta}$ ,  $0 \leq x \leq 1$ , is an interesting system spanning the range from slightly iron-doped  $\text{SrTiO}_3$  as a model representative of acceptor-doped large band gap electroceramics to iron-rich  $\text{Sr}(\text{Fe}_x\text{Ti}_{1-x})\text{O}_{3-\delta}$  materials which are good electronic and ionic conductors. Such mixed conductors can serve as key functional materials in fuel cells, electrochemical sensors, permeation membranes, and catalysts. In  $\text{Sr}(\text{Fe}_x\text{Ti}_{1-x})\text{O}_{3-\delta}$ , the iron substitutes for  $\text{Ti}^{4+}$  partly in the oxidation state of  $\text{Fe}^{3+}$  and partly as  $\text{Fe}^{4+}$ , the actual  $\text{Fe}^{3+}/\text{Fe}^{4+}$  fraction depending on total iron concentration, oxygen partial pressure  $p(\text{O}_2)$ , and temperature. The charge compensation for  $\text{Fe}^{3+}$  occurs predominantly by the formation of mobile oxygen vacancies  $V_{\text{O}}^{\bullet}$  (Kröger-Vink notation<sup>1</sup>). For low iron contents, the defect concentrations can be calculated from a defect model expressed in terms of ideal mass action laws.<sup>2</sup> Already for iron concentrations in the percent range, interaction of the charged defects leads to strong deviations from the dilute defect model. The formation of an iron impurity band occurs for iron concentrations of 3%–10% and represents a drastic change of the electronic structure.<sup>3,4</sup> Magnetism,<sup>5</sup> as well as related transport properties of these materials, has been the subject of intensive investigation.<sup>6,7</sup> For  $x \approx 0.3$ , the electrical resistance shows negligible temperature dependence in the  $p(\text{O}_2)$  range of  $10^{-4}$ –1 bar, which is interesting for resistive oxygen sensor applications.<sup>8</sup>

In this work, we present the dependence of the electronic and atomic structures of  $\text{Sr}(\text{Fe}_x\text{Ti}_{1-x})\text{O}_{3-\delta}$  perovskites on the composition, probed by x-ray diffraction (XRD), x-ray absorption spectroscopy (XAS), and vibrational (Raman and infrared) spectroscopy. The advance of XAS experimental techniques provides a chance to access the local environment around Fe centers throughout the whole  $\text{Sr}(\text{Fe}_x\text{Ti}_{1-x})\text{O}_{3-\delta}$  series. In this series, the electronic properties change drastically from isolated iron impurities hosted in a large band gap semiconductor to the metallic but strongly correlated  $\text{SrFeO}_3$ .<sup>9</sup> For dilute  $\text{Fe}^{4+}$  centers, a Jahn-Teller (JT) distortion

is predicted by quantum chemical calculations,<sup>3</sup> while the iron in  $\text{SrFeO}_3$  is known to have an undistorted octahedral coordination.<sup>9</sup> The transition between these limiting cases is addressed in this study.

## II. EXPERIMENT

$\text{Sr}(\text{Fe}_x\text{Ti}_{1-x})\text{O}_{3-\delta}$  powder samples were prepared from  $\text{SrCO}_3$ ,  $\text{TiO}_2$ , and  $\text{Fe}_2\text{O}_3$  powders by heating first to 1200 °C and then three times to 1300 °C in air with intermittent grinding in a zirconia ball mill. Fully reduced samples ( $\delta=x/2$ ) were prepared by heating for 2 h with 8%  $\text{H}_2$  in  $\text{N}_2$  at 700 °C followed by rapid quenching. Thermogravimetry (TG) showed that these conditions are sufficient to reduce all Fe ions to  $\text{Fe}^{3+}$ . Fully oxidized samples, i.e., stoichiometric samples with  $\delta=0$ , were prepared by a high oxygen pressure treatment at 600 bars and temperature decrease from 550 to 180 °C with the cooling rate decreasing from 40 to 1 K/h. The oxygen stoichiometry of the oxidized  $\text{Sr}(\text{Fe}_x\text{Ti}_{1-x})\text{O}_3$  samples with  $x \geq 0.03$  was checked by TG: heating in 8%  $\text{H}_2/\text{N}_2$  to 700 °C leads to complete reduction of all iron to  $\text{Fe}^{3+}$  (for buoyancy corrections, the empty sample holder was measured under the same conditions). All samples were found to be more than 95% oxidized; only  $x=0.5$  exhibits a slightly lower value of 93%. For samples with  $x \geq 0.3$ , iodometric titrations yielded degrees of oxidation  $\geq 95\%$ . The results are summarized in Table I.

XRD patterns were measured at room temperature using the Cu  $K\alpha$  radiation in Bragg-Brentano geometry with internal Si standard in the range  $2\theta=10^\circ$ – $120^\circ$  (Fig. 1). All oxidized samples and the reduced samples with  $x < 0.9$  were found to be single phase cubic  $\text{ABO}_3$  perovskites (space group  $Pm\bar{3}m$ ), while the reduced ones with  $x=0.9$  and  $x=1$  were predominantly or purely of brownmillerite structure<sup>10</sup> (space group  $Ibm2$ ). Lattice parameters were refined by least squares minimization using the program LCLSQ<sup>11</sup> after indexing with the program DICVOL91.<sup>12</sup>

Fe and Ti  $K$ -edge XAS spectra were measured at the ESRF synchrotron (Grenoble, France) at the BM29 beam

TABLE I. Degree of oxidation of oxidized  $\text{Sr}(\text{Fe}_x\text{Ti}_{1-x})\text{O}_3$  samples determined by TG and iodometric titration.

Fe content $x$	Thermogravimetry (%)	Titration (%)
0.03	$100 \pm 10$	
0.1	$100 \pm 5$	
0.2	$96 \pm 5$	
0.3	$95 \pm 2$	$95 \pm 3$
0.5	$93 \pm 2$	$96 \pm 3$
0.75	$98 \pm 2$	$102 \pm 3$
0.9	$96 \pm 2$	$102 \pm 3$
1.0	$98 \pm 2$	$101 \pm 3$

line.<sup>13</sup> Storage ring energy and average current were 6.0 GeV and 200 mA, respectively. The synchrotron radiation was monochromatized using a Si(111) double crystal monochromator. The harmonic rejection, with rejection level better than  $10^{-5}$ , is achieved using a double reflection on a pair of Si mirrors with grazing incidence of 3 and 5 mrad for Fe and Ti  $K$  edges, respectively. The energy resolution  $\Delta E/E$  was about  $2 \times 10^{-4}$ . The Ti  $K$ -edge spectra and the Fe  $K$ -edge spectra for  $x \geq 0.1$  were recorded in transmission mode by two ionization chambers filled with nitrogen gas with a rate of 1–4 s per point. The Fe  $K$ -edge spectra for  $x=0.01$  and  $x=0.03$  were performed in fluorescence mode using a 13-element Ge solid state detector with a rate of 4 s per point. Low temperature XAS measurements were performed in the range from 20 to 350 K using a closed-loop liquid helium cryostat with a heating resistor. The temperature during each measurement was stabilized within 2 K. The powder samples were deposited on Millipore filters and fixed by Kapton tape. The obtained sample thickness corresponded to an absorption jump  $\Delta\mu_x=0.12$ – $0.72$  at the Fe  $K$  edge and  $0.31$ – $1.0$  at the Ti  $K$  edge, depending on the composition.

Raman spectra were recorded on powder samples at room temperature with a Jobin-Yvon Labram V010 spectrometer [single monochromator equipped with a Notch filter and charge coupled device (CCD) camera] in backscattering geometry with excitation wavelengths of 632.8 and 784.7 nm and a power of 4 mW. Low temperature Raman spectra were

recorded on slightly compacted powder samples with a Dilor-XY triple monochromator spectrometer using a CCD camera in backscattering geometry at an excitation wavelength of 514.5 nm and a power of 10 mW. Infrared spectra (IR) were measured at room temperature in diffuse reflection mode on KBr diluted powder samples (3 mg in 400 mg KBr) with a Bruker IFS 66 spectrometer. The measured reflectivity  $R$  was transformed into the Kubelka-Munk function  $\text{KM} = (1-R)^2/(2R)$  which is proportional to the absorption coefficient.

### III. DATA ANALYSIS

X-ray absorption spectra at the Fe and Ti  $K$  edges were analyzed using the EDA software package.<sup>14</sup>

The x-ray absorption near edge structure (XANES) region at the Fe(Ti)  $K$  edge was separated from the total x-ray absorption coefficient by subtracting the preedge background and normalizing the absorption coefficient around 100 eV above the edge (Figs. 2 and 3). The XANES signals at both edges consist of the well visible preedge peak(s), the main absorption edge, and the fine structure above it.

The Fe(Ti)  $K$ -edge extended x-ray absorption fine structure (EXAFS) signals  $\chi(k)$  were extracted according to conventional definition as

$$\chi(k) = [\mu_{\text{expt}}(E) - \mu_0(E) - \mu_b(E)]/\mu_0(E), \quad (1)$$

where  $\mu_{\text{expt}}(E)$  is the experimental absorption coefficient,  $\mu_b(E)$  is the preedge background extrapolated beyond the absorption edge,  $\mu_0(E)$  is the atomiclike contribution, and  $k = [(2m_e/\hbar^2)(E - E_0)]^{1/2}$  is the wave vector, with  $E_0$  being the photoelectron energy origin.

The choice of correct  $E_0$  value is important, since it affects the amplitude and the phase of the EXAFS signal, especially at low  $k$  values, and therefore restricts the accuracy of interatomic distance determination. The best results were achieved when the  $E_0$  position in the experimental signal under study was set in the same way as for the reference signal, which can be either another experimental signal, measured for the reference compound with known crystallographic structure, or a theoretically calculated signal by one of the available *ab initio* codes.<sup>15–17</sup> In this work, the FEFF8 code<sup>15</sup> was used for generating the reference signal, and the

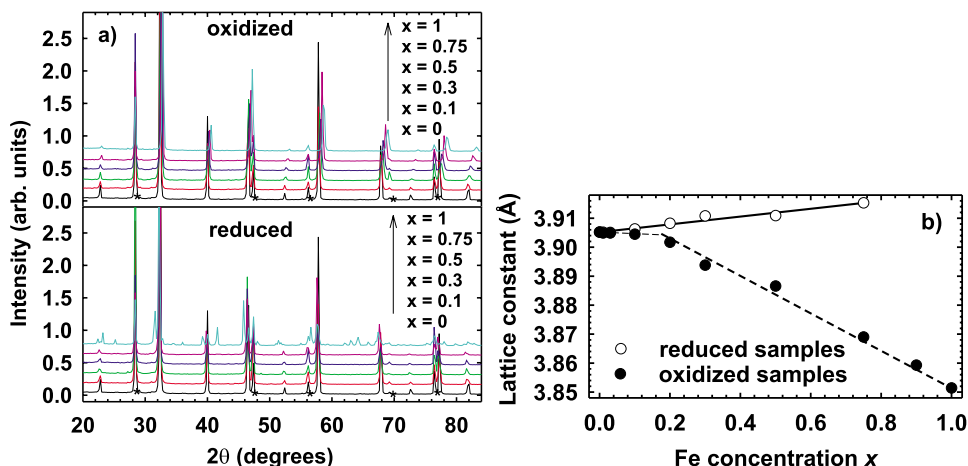


FIG. 1. (Color online) (a) Room temperature x-ray powder diffraction patterns for  $\text{Sr}(\text{Fe}_x\text{Ti}_{1-x})\text{O}_{3-\delta}$  samples. Stars denote the reflection from the internal Si standard; the peak splitting at high angles is due to  $\text{Cu } K\alpha_1 K\alpha_2$ . (b) Lattice constants obtained by XRD. Lines are drawn as a guide for the eye; the symbol size represents the error bar.

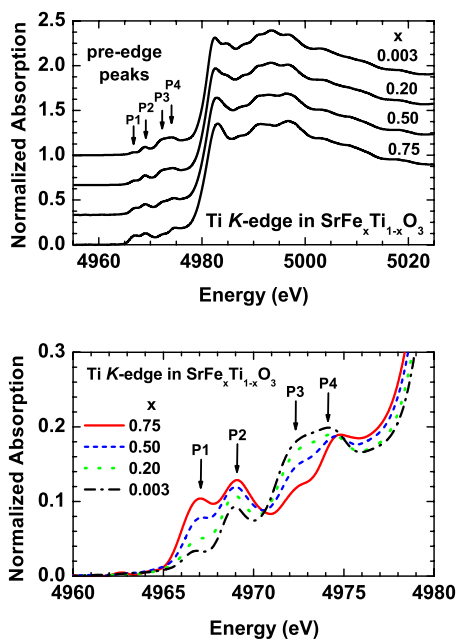


FIG. 2. (Color online) Upper panel: Ti *K*-edge XANES signals in oxidized Sr(Fe<sub>*x*</sub>Ti<sub>1-*x*</sub>)O<sub>3</sub> samples at room temperature. Only a few spectra are shown and are vertically shifted for clarity. Lower panel: enlarged preedge Ti *K*-edge XANES region.

$E_0$  position was set at 7117.0 eV for Fe<sup>4+</sup>, 7116.5 eV for Fe<sup>3+</sup>, and 4971.0 eV for Ti<sup>4+</sup> (Fig. 4). The FEFF8 code was also used for the interpretation of peak origin in Fourier transforms similar to our previous works.<sup>18,19</sup>

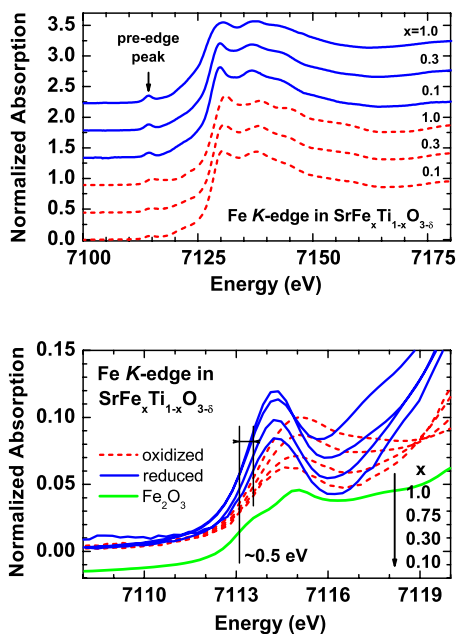


FIG. 3. (Color online) Upper panel: Fe *K*-edge XANES signals in oxidized (dashed curves) and reduced (solid curves) Sr(Fe<sub>*x*</sub>Ti<sub>1-*x*</sub>)O<sub>3- $\delta$</sub>  samples at room temperature. Only a few spectra are shown and are vertically shifted for clarity. Lower panel: enlarged preedge Fe *K*-edge XANES region. The curve for  $\alpha$ -Fe<sub>2</sub>O<sub>3</sub> is shifted downward by -0.02 for clarity.

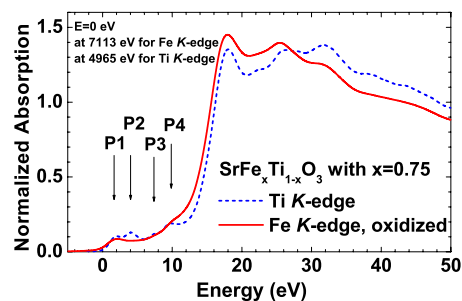


FIG. 4. (Color online) Comparison of the Ti and Fe *K*-edge XANES signals of oxidized Sr(Fe<sub>*x*</sub>Ti<sub>1-*x*</sub>)O<sub>3</sub> ( $x=0.75$ ) sample. The energy scale of the two spectra was aligned relative to the absorption threshold.

The experimental Fe(Ti) *K*-edge EXAFS signals  $\chi(k)k^2$  and their Fourier transforms (FTs) for fully oxidized and reduced Sr(Fe<sub>*x*</sub>Ti<sub>1-*x*</sub>)O<sub>3- $\delta$</sub>  samples are shown in Figs. 5–7. The FTs were calculated in the  $k$ -space range from 0.5 to 15 Å<sup>-1</sup> (or less when limited by the signal quality) using the Kaiser-Bessel window function with parameter  $A=2$  as implemented in Ref. 14. Note that due to the presence of the scattering phase shifts, the positions of peaks in FTs generally differ from the true values. The first coordination shell around iron and titanium atoms was isolated by back-Fourier transformation (typically in the range from 0.8 to 2.1 Å) and analyzed by a best-fit procedure using the model described below. The fit procedure was done in  $k$  space using typically the range from 2 to 12 Å<sup>-1</sup>; however, for a few reduced samples, the range was shortened to  $k=2-8$  Å<sup>-1</sup> due to poor signal quality at high  $k$  values.

The first coordination shell EXAFS  $\chi(k)$  signal can be accurately described in the single-scattering curved-wave cumulant approximation as<sup>20</sup>

$$\chi(k) = \sum_i S_0^2 \frac{N_i}{kR_i^2} F_i(k, R_i) \exp \left[ -2\sigma_i^2 k^2 + \frac{2}{3} C_{4i} k^4 - \frac{4}{45} C_{6i} k^6 \right] \times \sin \left[ 2kR_i - \frac{4}{3} C_{3i} k^3 + \frac{4}{15} C_{5i} k^5 + \Phi_i(k, R_i) \right], \quad (2)$$

where  $i$  denotes the group of atoms inside the shell,  $N_i$  the coordination number,  $R_i$  the average distance, the mean square relative displacement (MSRD), corresponding to the thermal Debye-Waller factor in the absence of static distortions, and  $C_{3i}$ ,  $C_{4i}$ ,  $C_{5i}$ , and  $C_{6i}$  the higher order cumulants of the distance distribution. In this work, we used two single-component models: (1) Gaussian approximation with only three ( $N, R, \sigma^2$ ) fitting parameters and (2) cumulant approximation with four ( $N, R, \sigma^2, C_3$ ) fitting parameters which improves the fit in some cases without affecting significantly the results and conclusions. The amplitude  $F_i(k, R_i)$  and phase shift  $\Phi_i(k, R_i)$  functions for the Fe-O and Ti-O atom pairs were calculated with the FEFF8 code<sup>15,21</sup> using the complex exchange-correlation Hedin-Lundqvist potential. The calculations were performed for a cluster with radius of 8 Å having the structure of cubic SrFeO<sub>3</sub>(SrTiO<sub>3</sub>) and centered at the Fe(Ti) atom, respectively. Calculations of the cluster po-

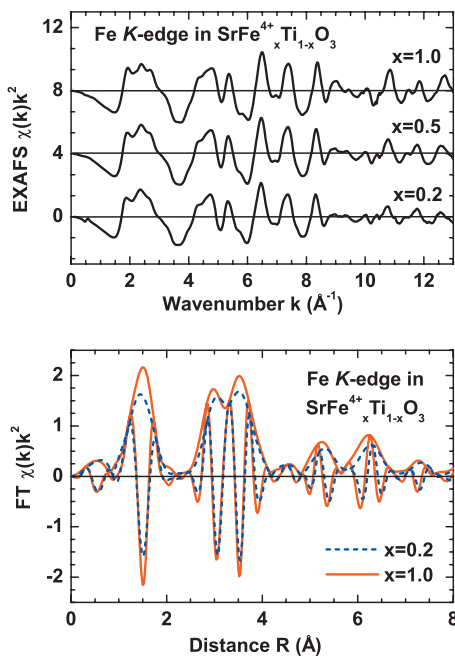


FIG. 5. (Color) Iron concentration dependence of experimental Fe  $K$ -edge EXAFS signals  $\chi(k)k^2$  and their Fourier transforms in fully oxidized  $\text{Sr}(\text{Fe}_x\text{Ti}_{1-x})\text{O}_3$  samples at room temperature. Only a few spectra are shown for clarity.

tentials were done in the *muffin-tin* (MT) self-consistent-field approximation using default values of MT radii as provided within the FEFF8 code.<sup>15</sup>

The value of the amplitude reduction factor  $S_0^2$  due to many-body effects was estimated to be 0.67 for both Fe and Ti  $K$  edges based on known coordination numbers of end

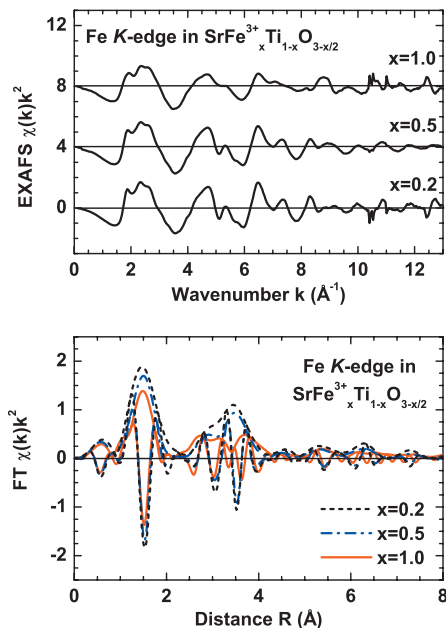


FIG. 6. (Color) Concentration dependence of experimental Fe  $K$ -edge EXAFS signals  $\chi(k)k^2$  and their Fourier transforms in fully reduced  $\text{Sr}(\text{Fe}_x^{3+}\text{Ti}_{1-x})\text{O}_{3-x/2}$  samples at room temperature. Only a few spectra are shown for clarity. Note that the sample with  $x=1$  has brownmillerite structure.

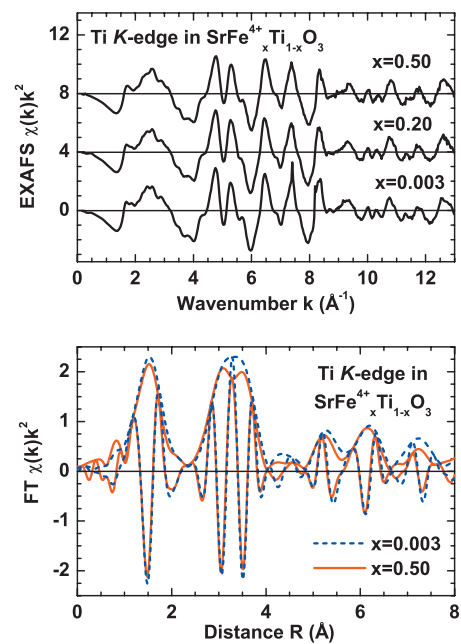


FIG. 7. (Color) Concentration dependence of experimental Ti  $K$ -edge EXAFS signals  $\chi(k)k^2$  and their Fourier transforms in fully oxidized  $\text{Sr}(\text{Fe}_x^{4+}\text{Ti}_{1-x})\text{O}_3$  samples at room temperature. Only a few spectra are shown for clarity.

members  $\text{SrTiO}_3$  and  $\text{SrFeO}_3$ . Note that this value of  $S_0^2$  is close to the one (0.69) found for  $\text{SrFe}_x\text{Sn}_{1-x}\text{O}_{3-y}$  in Ref. 22. The distances determined in the fitting procedure, Fig. 9, were brought in accord with the distances known from XRD data for  $\text{SrTiO}_3$  and  $\text{SrFeO}_3$  (Ti and Fe  $K$  edges, respectively) by a constant shift of 0.02 Å.

The error bars were estimated based on the largest data scatter appearing in due course of analysis.

## IV. RESULTS

### A. X-ray absorption near edge structure

The XANES signals at the Fe and Ti  $K$  edges in  $\text{Sr}(\text{Fe}_x\text{Ti}_{1-x})\text{O}_{3-\delta}$  samples reveal qualitative similarity but differ in details although iron and titanium occupy the same crystallographic site and have scattering amplitudes close enough. A group of four preedge peaks is observed at the Ti  $K$  edge (Fig. 2), whereas a single broad peak is visible at the Fe  $K$  edge (Fig. 3; the edge region of  $\text{Fe}_2\text{O}_3$  is shown for comparison). Two effects can be emphasized: (i) The intensity of the preedge peaks varies with composition, see Sec. V. (ii) For the Fe  $K$  edge, the preedge peak intensity is slightly higher in reduced samples for the same composition, and there is an energy difference of about 0.5 eV between the edges of the first preedge peaks in oxidized and reduced samples. The reason for this small shift is the large covalency of the  $\text{Fe}^{4+}\text{-O}^{2-}$  bonds (corresponding to a heavy admixture of the  $d^5\bar{L}$  states;  $\bar{L}$  means a hole in oxygen  $2p$  orbitals)<sup>23,24</sup> which reduces the charge on  $\text{Fe}^{4+}$ . Note also that the edge energy position (7113 eV) of the first preedge peak for reduced samples is in good agreement with that for  $\text{Fe}_2\text{O}_3$ , having all iron ions in  $3+$  valence state.

The XANES signal is due to transitions (allowed by selection rules) to unoccupied electronic states, which are relaxed in the presence of the core hole. In the case of the Fe and Ti *K* edges, the main x-ray absorption occurs due to the dipole-allowed excitation of the 1*s* electron to states with *p* character.<sup>25–28</sup> The preedge transitions, which probe the unoccupied states in the conduction band region, are more difficult to explain. Different authors attribute these peaks to transitions of different characters: a pure dipole-allowed 1*s*→*np* model was suggested in Refs. 26 and 28, a pure quadrupole origin was accepted in Ref. 22, whereas a mixed dipole-quadrupole origin was favored in Refs. 25, 27, and 29–31. Note that the value of the transition matrix elements for the quadrupole transition is only about 1% of that for the dipole transition, however, this difference can be compensated by the larger number of available 3*d* states.<sup>32</sup> The situation is even more complicated because the dipole character of the preedge peaks has also been proposed to be of different origin.<sup>25–28,33,34</sup> To conclude, there are several interpretations based on different theoretical approaches and approximations, which makes the unique explanation of the preedge peaks rather complicated.

The Ti *K*-edge XANES in pure SrTiO<sub>3</sub> has been studied in Refs. 25–27. While all groups were able to interpret experimental data reasonably well, they provide different explanations of the preedge peak origin. Further, we will follow the interpretation provided in Refs. 30 and 31 for the Ti *K* edge in TiO<sub>2</sub>, which exhibits a preedge peak structure very similar to Sr(Fe<sub>*x*</sub>Ti<sub>1–*x*</sub>)O<sub>3–*δ*</sub> due to octahedral coordination of titanium atoms in both compounds. The first preedge peak P1 in Fig. 2 was assigned to pure quadrupole origin due to 1*s*(Ti)→3*d*(*t*<sub>2*g*</sub>)(Ti) transition,<sup>30</sup> in agreement also with Refs. 25 and 27. The second peak P2 is dipolar in nature, being mainly due to 1*s*(Ti)→4*p*(Ti) transition but includes some degree of 1*s*(Ti)→3*d*(*e*<sub>*g*</sub>)(Ti) quadrupole contribution.<sup>27,30</sup> Both quadrupole contributions predicted in Ref. 30 have been experimentally confirmed.<sup>31</sup> It was suggested<sup>25</sup> that the intensity of the Ti *K*-edge peak P2 is proportional to a displacement of Ti atoms from the center of the TiO<sub>6</sub> octahedra but inversely related to the Ti-O bond length. Finally, the next two preedge peaks P3 and P4 are due to pure 1*s*(Ti)→4*p*(Ti) dipole transitions.<sup>25–27,30</sup>

To understand the Fe *K* preedge, we first compare the Fe and Ti *K*-edge XANES signals (Fig. 4) in oxidized Sr(Fe<sub>0.75</sub>Ti<sub>0.25</sub>)O<sub>3</sub>. After aligning both XANES spectra relative to the absorption threshold, we note a good correspondence between the main absorption maxima located at 18 eV. The main features at higher energies, determined by the frequency of the EXAFS oscillations, are in close correspondence, indicating the expected similarity of the local structure around Ti and Fe. However, in contrast to the Ti *K* edge, the preedge structures at the Fe *K* edge are less resolved. Taking into account the similarity of two XANES signals, one can suppose a similar origin of the preedge peaks. We attribute the peak at 7115 eV in Fig. 3 (peak P1 in Fig. 4) to 1*s*(Fe)→3*d*(Fe) quadrupole transition and the shoulder at 7122 eV (P4 in Fig. 4) to pure 1*s*(Fe)→4*d*(Fe) dipole transition. The intermediate features at about 7116–7120 eV can be correlated with transitions having

both 1*s*(Fe)→3*d*(Fe) quadrupole and 1*s*(Fe)→4*d*(Fe) dipole character. On the basis of these assignments, a correlation between the variations of the prepeaks and the local environment around Fe/Ti ions will be discussed in Sec. V.

## B. Extended x-ray absorption fine structure and x-ray diffraction

Experimental Fe and Ti *K*-edge EXAFS signals  $\chi(k)k^2$  and their FTs of oxidized and reduced Sr(Fe<sub>*x*</sub>Ti<sub>1–*x*</sub>)O<sub>3–*δ*</sub> samples are shown in Figs. 5–7. Note that all obtained EXAFS  $\chi(k)k^2$  signals have a very good signal to noise ratio up to 12 Å<sup>–1</sup>. The FTs of the EXAFS signals are typical for the perovskite-type structure<sup>18</sup> and exhibit a number of well resolved peaks up to 8 Å. In this work, we concentrate mainly on the analysis of the first peak at about 1.5 Å, which is isolated well and corresponds to the first coordination shell of Fe(Ti) atoms. In “stoichiometric,” i.e., fully oxidized Sr(Fe<sub>*x*</sub><sup>4+</sup>Ti<sub>1–*x*</sub>)O<sub>3</sub>, the first shell is composed of six oxygen atoms, whereas some decrease of the coordination number can be expected in reduced samples due to the presence of oxygen vacancies.

The analysis of peaks beyond the first shell is a more demanding task due to the overlap of contributions from outer coordination shells and additional complications caused by strong multiple-scattering effects, mainly in linear atomic chains such as *B*–*O*–*B* and *O*–*B*–*O* (*B*=Fe or Ti).<sup>18</sup> However, qualitative comparison of FTs allows us to draw some conclusions. In cubic perovskite-type compounds, the amplitude of the peak corresponding to the second coordination shell (the peak at 3.5 Å in Figs. 5 and 7) depends strongly on the bond angle *B*–*O*–*B* between two *BO*<sub>6</sub> octahedra.<sup>18,35</sup> In oxidized cubic Sr(Fe<sub>*x*</sub><sup>4+</sup>Ti<sub>1–*x*</sub>)O<sub>3</sub>, this peak is strong at both Fe and Ti *K* edges, being comparable in amplitude with the first shell peak at 1.5 Å and varies slightly with composition due to the lattice parameter variation. At the same time, the peak at 3.5 Å in reduced Sr(Fe<sub>*x*</sub><sup>3+</sup>Ti<sub>1–*x*</sub>)O<sub>3–*x*/2</sub> has a nearly two times smaller amplitude than the first shell (Fig. 6) for low iron content; moreover, it becomes even smaller for *x*=1.0 when Sr(Fe<sub>*x*</sub><sup>3+</sup>Ti<sub>1–*x*</sub>)O<sub>3–*x*/2</sub> transforms to the brownmillerite phase.<sup>10</sup> Such a behavior usually indicates a deviation of the *B*–*O*–*B* angles from linear configuration due to rotations of *BO*<sub>6</sub> octahedra or off-center displacement of metal ions. Similar effects have been observed in many perovskite-type compounds, e.g., in tungsten oxides<sup>36</sup> upon a change of stoichiometry or in ReO<sub>3</sub> (Ref. 37) upon pressure variation. Another possible explanation can be a strong increase of the static or thermal disorder, as has been observed in ReO<sub>3</sub> (Ref. 19) upon heating. Note that the peaks due to outer shells in reduced Sr(Fe<sub>*x*</sub><sup>3+</sup>Ti<sub>1–*x*</sub>)O<sub>3–*x*/2</sub>, located at distances above 4 Å in Fig. 6, have also much smaller amplitudes than analogous peaks in oxidized Sr(Fe<sub>*x*</sub><sup>4+</sup>Ti<sub>1–*x*</sub>)O<sub>3</sub> (Figs. 5 and 7). This suggests the presence of long nonlinear *B*–*O*–*B*–*O*–*B* chains in reduced samples, and thus a possible deviation of their local structure from cubic symmetry due to the presence of oxygen vacancies.

The results of the fitting of the first *B*–*O* coordination shell are shown in Figs. 8–10. In the stoichiometric prov-

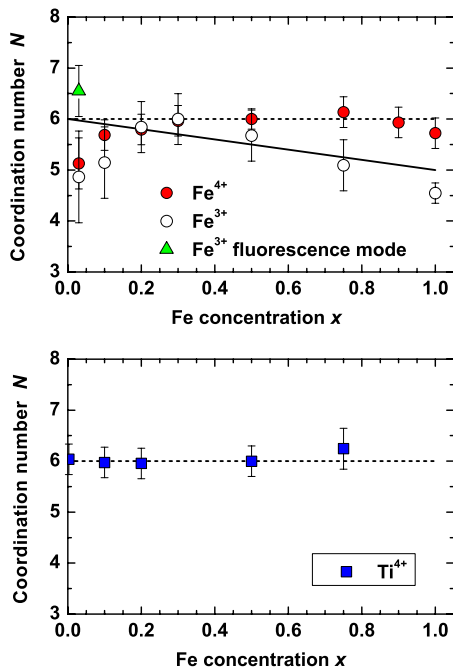


FIG. 8. (Color online) Concentration dependence of the coordination numbers around  $\text{Fe}^{4+}$  and  $\text{Ti}^{4+}$  in  $\text{Sr}(\text{Fe}_x^{4+}\text{Ti}_{1-x})\text{O}_3$  oxidized samples, and  $\text{Fe}^{3+}$  in  $\text{Sr}(\text{Fe}_x^{3+}\text{Ti}_{1-x})\text{O}_{3-x/2}$  reduced samples in the first coordination shell, all at room temperature. Dashed lines correspond to the octahedral coordination of the  $\text{Fe}^{4+}$  ( $\text{Ti}^{4+}$ ) ions in the stoichiometric perovskite. Solid line indicates the expected coordination for  $\text{Fe}^{3+}$  ions in the presence of oxygen vacancies.

skite structure, the coordination number of oxygen (Fig. 8) around the Fe as well as the Ti cation is 6 for the fully oxidized samples. This fact was used as the reference point to determine the values of  $S_0^2$  mentioned in Sec. III. Using these values, a decrease of the coordination number around  $\text{Fe}^{3+}$  is observed for the completely reduced samples having large iron concentrations, while the large error bars at low  $x$  (due to the increased noise in the spectra) do not allow a safe conclusion for the low doped samples. The electroneutrality condition requires the oxygen vacancy concentration to be equal to half of the  $\text{Fe}^{3+}$  concentration. In dilute systems with isolated Fe ions, this means that even if the electrostatic attraction of the oppositely charged defects is strong, only half of the  $\text{Fe}^{3+}$  can have a  $\text{V}_\text{O}^\bullet$  in the first coordination shell. For  $x \leq 0.003$ , electron paramagnetic resonance measurements show that the tendency for a  $\text{V}_\text{O}^\bullet$  to be located in the first coordination shell of  $\text{Fe}^{3+}$  ( $\text{Fe}_\text{Ti}^\bullet$ ) (Ref. 1) decreases with increasing iron content.<sup>38</sup> For large  $x$ ,  $\text{Fe}_\text{Ti}^\bullet - \text{V}_\text{O}^\bullet$  pairs are unavoidable if Fe and Ti are randomly distributed (there is no evidence for an Fe/Ti ordering): for  $x=0.5, 0.25$  oxygens per B cation are missing, and since each belongs to two octahedra, in every second octahedron, an oxide ion is absent. This leads to expected coordination numbers for  $\text{Fe}^{3+}$  of 5.5 ( $x=0.5$ ) and 5.25 ( $x=0.75$ ), which agree with the experimental findings within the error bars (a distribution of the  $\text{V}_\text{O}^\bullet$  between octahedrally and fourfold coordinated  $\text{Fe}^{3+}$  as concluded from Mössbauer spectra would result in the same averaged coordination numbers, see, e.g., Refs. 39 and 40). The deviation observed for  $x=1$  from the value of 5 expected for

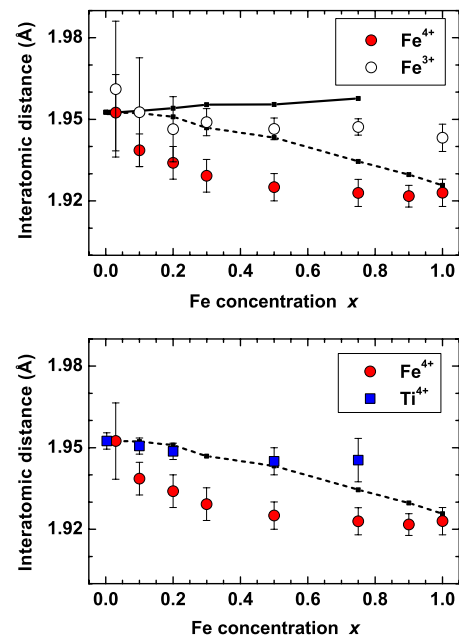


FIG. 9. (Color online) Concentration dependence of the  $\text{Fe}^{4+}-\text{O}^{2-}$  and  $\text{Ti}^{4+}-\text{O}^{2-}$  (oxidized samples) and  $\text{Fe}^{3+}-\text{O}^{2-}$  (reduced samples) distances in the first coordination shell, all at room temperature. The half-values of the lattice constants obtained by XRD are shown for comparison: dashed curve for oxidized and solid curve for reduced samples.

the brownmillerite structure must be due to experimental errors. The coordination number of O around Ti is also expected to fall below 6 for the reduced samples with large  $x$ ; unfortunately, these measurements are missing because of limited beam time.

Figure 9 shows the average (Fe, Ti)-O distances determined from XRD (half value of the lattice constant) and EXAFS (local Fe-O and Ti-O distances). From the Shannon ionic radii,<sup>41</sup> the substitution of  $\text{Ti}^{4+}$  ( $r=0.605 \text{ \AA}$  in octahedral coordination) by  $\text{Fe}^{3+}$  ( $r=0.645 \text{ \AA}$ ) is expected to increase the lattice constant, whereas  $\text{Fe}^{4+}$  ( $r=0.585 \text{ \AA}$ ) should decrease it. As Fig. 9 shows, these general trends are indeed observed in the XRD data. The lattice parameter remains constant for  $x \leq 0.15$  and then decreases linearly with in-

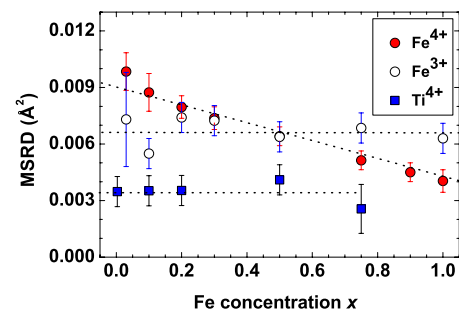


FIG. 10. (Color online) Concentration dependence of the MSRD for  $\text{Fe}^{4+}-\text{O}^{2-}$  and  $\text{Ti}^{4+}-\text{O}^{2-}$  bonds (oxidized samples) and  $\text{Fe}^{3+}-\text{O}^{2-}$  bonds (reduced samples) in the first coordination shell, all at room temperature. Dotted lines are guides for the eye.

creasing  $x$ . This deviation from Vegard's law can be rationalized as follows: The Ti<sup>4+</sup> in SrTiO<sub>3</sub> is slightly too small for its octahedral site (the Goldschmidt tolerance factor  $t = (r_A + r_O) / [\sqrt{2}(r_B + r_O)] = 1.002$  is larger than unity; the facile displacement of Ti<sup>4+</sup> inside the O<sub>6</sub> octahedron gives rise to the high relative dielectric constant  $\epsilon_r \approx 300$  at room temperature). Therefore, the lattice parameter is determined essentially by close packing of the Sr<sup>2+</sup> and O<sup>2-</sup> ions. Substituting Ti<sup>4+</sup> by the smaller Fe<sup>4+</sup> can decrease the lattice parameter only indirectly, i.e., by withdrawing electron density from the O<sup>2-</sup> ions which reduces their size. Obviously, this occurs only for  $x \geq 0.15$ .

The lattice constants for Sr(Fe<sub>*x*</sub>Ti<sub>1-*x*</sub>)O<sub>3- $\delta$</sub>  samples reported in Ref. 6 seem to be questionable since for  $x \rightarrow 0$ , they do not approach the SrTiO<sub>3</sub> value of 3.905 Å but rather 3.915 Å. The Sr(Fe<sub>*x*</sub>Ti<sub>1-*x*</sub>)O<sub>3- $\delta$</sub>  samples studied in Ref. 5 were prepared by a different  $p(\text{O}_2)$ -temperature scheme than the samples in this work, and thus cannot be compared directly. The lattice parameters in Ref. 5 also show deviations from Vegard's law which could be, at least partly, due to incomplete oxidation (the Mössbauer spectra indicate oxygen deficiency for samples with intermediate  $x$ ), but nevertheless exhibit the correct values for  $x \rightarrow 0$  and  $x \rightarrow 1$ .

The local distances determined by EXAFS analysis exhibit a more detailed picture with different Ti-O and Fe-O distances for the same sample. For the oxidized samples, the Ti-O distance remains essentially constant, at about 1.95 Å (the same as in SrTiO<sub>3</sub>), while the Fe-O distances stay close to that in SrFeO<sub>3</sub> (1.92 Å) for large  $x$  and increase only for  $x \leq 0.3$ . The composition variation of the Fe(Ti)-O distances, determined by EXAFS, deviates from the half-values of the lattice constants obtained by XRD (Fig. 9). Although the "fully oxidized" samples still contain a minor oxygen deficiency (see Table I), the small fraction of Fe<sup>3+</sup> is not sufficient to explain the increasing Fe-O distances just by averaging constant contributions from Fe<sup>4+</sup>-O and Fe<sup>3+</sup>-O (e.g., for  $x=0.1$ , about half of the Fe would have to be Fe<sup>3+</sup> to yield the observed Fe-O distance). For the reduced samples, we found nearly constant Fe-O distances of about 1.95 Å, which is slightly shorter at high iron content than the half-values of the lattice constants obtained by XRD (Fig. 9) (no Ti EXAFS data are available for these samples). Individual local EXAFS distances different from the averaged XRD value were also observed in other solid solution series, e.g., in Ca(Zr<sub>*x*</sub>Ti<sub>1-*x*</sub>)O<sub>3</sub> ( $0 \leq x \leq 1$ , samples calcined at 1200 °C)<sup>42</sup> or (Fe<sub>*x*</sub>Mn<sub>1-*x*</sub>)Nb<sub>2</sub>O<sub>6</sub> ( $0 \leq x \leq 1$ ).<sup>43</sup>

Figure 10 shows the MSRDS at room temperature for Fe<sup>4+</sup>-O<sup>2-</sup>, Fe<sup>3+</sup>-O<sup>2-</sup>, and Ti<sup>4+</sup>-O<sup>2-</sup> bonds (note that the EXAFS MSRDS models the disorder in the B-O bond length, while the Debye-Waller factor used in XRD describes the disorder of an atom around its equilibrium lattice position). The MSRDS of Fe<sup>3+</sup>-O<sup>2-</sup> (reduced samples) is to a good approximation independent of the iron concentration. The same behavior is observed for the MSRDS of Ti<sup>4+</sup>-O<sup>2-</sup> (oxidized samples). Most interestingly, the MSRDS of Fe<sup>4+</sup>-O<sup>2-</sup> exhibits a strong decrease with an increase of iron concentration, such that it is larger than the Fe<sup>3+</sup>-O<sup>2-</sup> MSRDS for small  $x$ , lower than that for large  $x$ , and finally, in SrFeO<sub>3</sub>, achieving about the same value as the Ti<sup>4+</sup>-O<sup>2-</sup> MSRDS in all samples. An

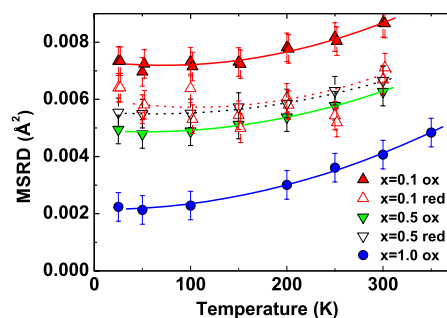


FIG. 11. (Color online) Temperature dependence of the MSRDS for Fe<sup>4+</sup>-O<sup>2-</sup> bonds (oxidized samples, solid symbols) and Fe<sup>3+</sup>-O<sup>2-</sup> bonds (reduced samples, open symbols) in the first coordination shell. Lines are guides for the eye.

$x=0.75$  sample prepared with deliberately incomplete oxidation (SrFe<sub>0.75</sub>Ti<sub>0.25</sub>O<sub>2.906</sub> instead of SrFe<sub>0.75</sub>Ti<sub>0.25</sub>O<sub>3</sub>) has a MSRDS slightly below that of the reduced sample. This demonstrates that the mixed valence of the Fe does not increase the Fe-O MSRDS above the value of the reduced samples. In the above mentioned EXAFS studies of Ca(Zr<sub>*x*</sub>Ti<sub>1-*x*</sub>)O<sub>3</sub> (Ref. 42) and (Fe<sub>*x*</sub>Mn<sub>1-*x*</sub>)Nb<sub>2</sub>O<sub>6</sub>,<sup>43</sup> the Ti-O and Zr-O MSRDS (Ref. 42) and the Fe-O and Mn-O MSRDS (Ref. 43) remain essentially constant throughout the whole solid solution series.

The temperature dependence of the Fe-O MSRDS of some samples is shown in Fig. 11. As expected, the MSRDS decreases as temperature decreases and remains approximately constant below 100 K. Even for SrFeO<sub>3</sub> where no disorder due to Fe/Ti substitution, JT distortion, and oxygen vacancies are expected, the temperature dependence cannot be quantitatively described by correlated Einstein<sup>44</sup> or correlated Debye<sup>45</sup> models. The failure of these simple models is not surprising since lattice dynamics calculations for SrTiO<sub>3</sub> (Ref. 46) yield phonon spectra that can be described neither by a single frequency nor by a Debye-type frequency distribution. The slope of the Fe<sup>4+</sup>-O<sup>2-</sup> MSRDS versus temperature observed for SrFeO<sub>3</sub> ( $1.33 \times 10^{-5} \text{ Å}^2/\text{K}$  in the range of 200–350 K) is comparable to the Ti<sup>4+</sup>-O<sup>2-</sup> MSRDS value determined for SrTiO<sub>3</sub> in the high temperature region ( $1.2 \times 10^{-5} \text{ Å}^2/\text{K}$  in the range of 200–1000 K).<sup>47</sup> Although a quantitative model for the temperature dependence of MSRDS is not available yet, Fig. 11 shows that there is a strong static disorder contribution, increasing with decreasing iron content. The temperature-dependent vibrational contribution is of comparable magnitude for different compositions, being only slightly higher for SrFeO<sub>3</sub>.

### C. Vibrational spectroscopy

The peak positions in the IR spectra of the oxidized Sr(Fe<sub>*x*</sub>Ti<sub>1-*x*</sub>)O<sub>3</sub> samples (Fig. 12) hardly change with increasing iron concentration. This finding is not unexpected since substitution of Fe<sup>4+</sup> for Ti<sup>4+</sup> should not drastically alter the force constant and the reduced mass (the observed peaks involve mainly B-O motions with the reduced mass being close to that of oxygen). However, for the reduced Sr(Fe<sub>*x*</sub>Ti<sub>1-*x*</sub>)O<sub>3-*x/2*</sub> samples, a splitting of the peak centered at

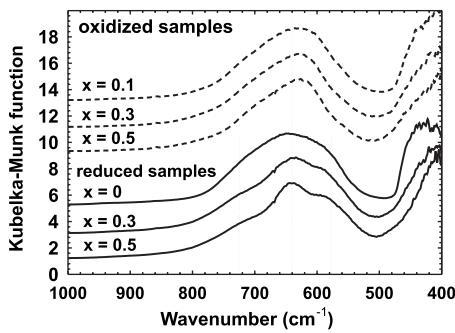


FIG. 12. Diffuse reflection infrared spectra for fully oxidized (top panel) and fully reduced (lower panel)  $\text{Sr}(\text{Fe}_x\text{Ti}_{1-x})\text{O}_{3-\delta}$  samples (for  $x=0$  the spectra of oxidized and reduced samples are identical). The spectra are scaled to comparable intensity at  $645\text{ cm}^{-1}$  and shifted upward for clarity. For oxidized samples with  $x>0.5$ , the high electronic conductivity of the samples impedes spectra acquisition.

$645\text{ cm}^{-1}$  into three components is found. The relative contribution of the  $645\text{ cm}^{-1}$  peak ( $\text{Ti}^{4+}\text{-O}^{2-}$  vibration) decreases with increasing iron concentration, while the component at  $590\text{ cm}^{-1}$  and the weaker shoulder at  $710\text{ cm}^{-1}$  gain weight ( $\text{Fe}^{3+}\text{-O}^{2-}$  vibrations).

In cubic perovskites, all first-order Raman lines are symmetry forbidden. Raman spectra for the oxidized and reduced samples are shown in Fig. 13. The broad structures at  $250\text{--}400$  and at  $600\text{--}800\text{ cm}^{-1}$  in pure  $\text{SrTiO}_3$  ( $x=0$ ) are due to second-order Raman scattering.<sup>49,51</sup> The  $\text{SrTiO}_3$  phonon modes,<sup>48–51</sup> determined, e.g., from hyper-Raman measurements, are indicated by vertical lines (LO4 and TO4 correspond to  $B\text{--}O$  stretching, and LO3 and TO3 to  $O\text{--}B\text{--}O$  bending modes). For the reduced  $\text{Sr}(\text{Fe}_x\text{Ti}_{1-x})\text{O}_{3-x/2}$  samples, the spectra become less structured with increasing iron con-

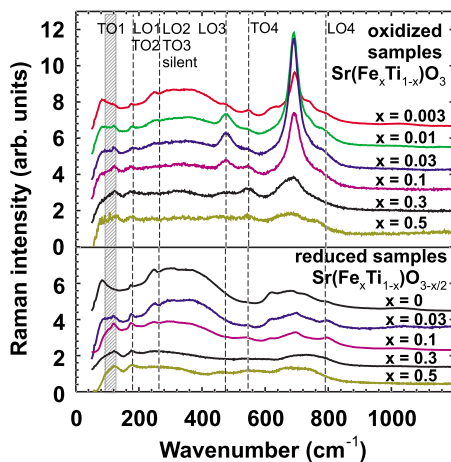


FIG. 13. (Color online) Raman spectra for fully oxidized (top panel) and fully reduced (lower panel)  $\text{Sr}(\text{Fe}_x\text{Ti}_{1-x})\text{O}_{3-\delta}$  samples (for  $x=0$ , the spectra of oxidized and reduced samples are identical). The spectra are scaled to comparable intensity in the  $200\text{--}400\text{ cm}^{-1}$  range and shifted upward for clarity. For samples with  $x>0.5$ , the high electronic conductivity of the samples impedes spectra acquisition. The positions of the  $\text{SrTiO}_3$  phonon modes classified following Refs. 48–51 are indicated by vertical lines.

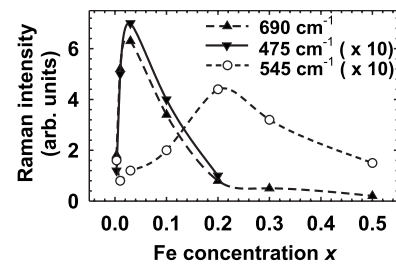


FIG. 14. Intensity of selected Raman peaks for fully oxidized  $\text{Sr}(\text{Fe}_x\text{Ti}_{1-x})\text{O}_3$  samples. For clarity, the values for the peaks at  $475$  and  $545\text{ cm}^{-1}$  are multiplied by a factor of 10.

centration. The substitution of  $\text{Fe}^{3+}$  for  $\text{Ti}^{4+}$  (which leads also to the appearance of oxygen vacancies located more or less close to the  $\text{Fe}^{3+}$  centers) represents a local symmetry lowering and could in principle lead to the appearance of Raman lines. For  $\text{SrTiO}_3$ , it is known that symmetry breaking by an applied electrical field<sup>48</sup> or the preparation of thin films<sup>52</sup> leads to the observation of first-order Raman peaks. The effect of  $B$ -site cation substitution was studied, e.g., for cubic  $\text{Sr}(\text{Mg}_{0.05}\text{Ti}_{0.95})\text{O}_{3-\delta}$  where a weak new peak at  $762\text{ cm}^{-1}$  was observed<sup>53</sup> and for orthorhombic  $\text{Ca}(\text{Zr}_x\text{Ti}_{1-x})\text{O}_3$  where a strong additional peak in the range of  $750\text{--}800\text{ cm}^{-1}$  was found for  $0.25 \leq x \leq 0.75$ .<sup>54</sup> In the spectra of the reduced samples  $\text{Sr}(\text{Fe}_x\text{Ti}_{1-x})\text{O}_{3-x/2}$ , even for large  $x$ , the presence of  $\text{Fe}^{3+}$  and oxygen vacancies obviously does not create a sufficient symmetry distortion for inducing pronounced Raman peaks. Spectra measured on oxygen vacancy containing  $\text{Sr}(\text{Sc}_{0.03}\text{Ti}_{0.97})\text{O}_{2.985}$  also do not show first-order Raman peaks.

For the oxidized  $\text{Sr}(\text{Fe}_x\text{Ti}_{1-x})\text{O}_3$  samples, a pronounced line at  $690\text{ cm}^{-1}$  appears at an iron concentration as low as  $x=0.003$ . Its intensity increases up to  $x=0.03$  and then decreases (Fig. 14). The full width at half maximum (FWHM) of the peak increases almost linearly from  $30\text{ cm}^{-1}$  ( $x=0.003$ ) to  $70\text{ cm}^{-1}$  ( $x=0.3$ ), while the peak position shifts only slightly to  $695\text{ cm}^{-1}$  for large  $x$ . For  $x=0.03$ , a systematic decrease of the  $690\text{ cm}^{-1}$  peak was observed for samples with a smaller degree of oxidation (prepared by heating to  $500\text{ }^\circ\text{C}$  in air or  $700\text{ }^\circ\text{C}$  in  $\text{N}_2$ ; spectra not shown). Since all these peaks are observed with the same frequencies and intensities for all applied excitation wavelengths ( $784.7$ ,  $632.8$ , and  $514.5\text{ nm}$ ), luminescence effects are not the origin of these lines. The fact that the frequency of  $690\text{ cm}^{-1}$  does not split into TO and LO modes and does not correspond to any of the  $\text{SrTiO}_3$  first-order phonons can be seen as an indication that this peak is caused by a vibration with local character. For such a local vibration, also modes with inversion symmetry at the  $\text{Fe}^{4+}$  center would become Raman active. On the other hand, the symmetry reduction at the  $\text{Fe}^{4+}$  also makes the LO3, TO4, and LO4 modes weakly allowed. The intensity at the  $475\text{ cm}^{-1}$   $\text{SrTiO}_3$  phonon frequency (and also of the shoulder at  $795\text{ cm}^{-1}$  which is difficult to quantify) increases in parallel to the  $690\text{ cm}^{-1}$  peak, while the intensity at  $545\text{ cm}^{-1}$  exhibits a broad maximum centered around  $x=0.2$ .

Low temperature measurements have been done for the oxidized  $\text{Sr}(\text{Fe}_{0.01}\text{Ti}_{0.99})\text{O}_3$  sample from room temperature

down to 120 K in steps of 20 K and an additional spectrum at 80 K bearing in mind the phase transition of SrTiO<sub>3</sub> into the tetragonal phase at 105 K (in first approximation, this does not change the character of the spectrum). The amplitude of the most pronounced peak at 690 cm<sup>-1</sup> increased by about 120% upon cooling, whereas the FWHM decreased by about 50% resulting in an overall peak intensity increase by about 20%.

## V. DISCUSSION

In this section, our experimental findings are discussed synoptically emphasizing the question of a JT distortion around Fe<sup>4+</sup> proposed in a recent theoretical study.<sup>3</sup> In the case of Fe<sup>3+</sup> ions, the high-spin ground state  $d^5(t_{2g}^3e_g^2)$  configuration<sup>55</sup> does not suppose any local structural distortion. Pure SrFeO<sub>3</sub> has Fe<sup>4+</sup> ( $d^4$ ) ions in high-spin configuration but has no JT distortion and exhibits metallic conductivity. These facts are explained by strong mixing of  $d^4(t_{2g}^3e_g)$  and  $d^5\bar{L}(t_{2g}^3e_g^2)$  configurations in the ground state that stabilizes the undistorted cubic perovskite structure and indicates a strong degree of covalency in the Fe-O bonds.<sup>23,24</sup> A local JT distortion can therefore be expected only for low iron concentrations where delocalization of the iron  $d$  electrons is not yet of influence. In this context, it is worth mentioning that  $x \approx 0.03$  marks the border between the low concentration regime with essentially independent Fe centers and the higher concentration regime where the formation of an iron impurity band begins<sup>3</sup> and the electronic conductivity significantly increases (together with the decrease in the activation energy for conductivity).<sup>4</sup>

While the origin of the XANES preedge peaks has been given above, we discuss here their composition dependence and their relationship with the EXAFS findings. The Ti-O MSDR (Fig. 10) and bond length (Fig. 9) are almost constant for all  $x$  in oxidized Sr(Fe <sub>$x$</sub> Ti <sub>$1-x$</sub> )O<sub>3</sub>, indicating similar degree of distortion around Ti<sup>4+</sup> ions. Therefore, one could expect<sup>25</sup> that the intensity of the peak P2 in Fig. 2 should not change with composition and its variation to be mostly connected with a variation of the background contribution from the neighboring peak P1. The P1 peak (quadrupole transition to  $3d$  states) decreases for lower iron content, and its intensity variation is larger at the Ti  $K$  edge (Fig. 2) than at the Fe  $K$  edge (Fig. 3). The change of the P1 intensity is determined by a variation of the squared transition matrix element and of the occupation number of  $3d$  metal states. Since the Ti environment does not change significantly, we do not expect the overlap integral to change. On the other hand, for large  $x$ , the stronger electron withdrawal from O<sup>2-</sup> to Fe<sup>4+</sup> can result in a decreased Ti  $3d$  occupation number. Note that the quadrupole transition at the Ti  $K$  edge is extremely sensitive to the occupation number.<sup>30</sup>

In the case of the P1 peak for Fe<sup>4+</sup>, the decrease of the Fe<sup>4+</sup>-O<sup>2-</sup> distances with increasing  $x$  might be viewed as an indication for "more compact"  $3d$  orbitals which leads to an increase of the overlap integrals, and thus to the P1 peak intensity increase with increasing  $x$ . However, in the case of Fe<sup>3+</sup> ions, the Fe<sup>3+</sup>-O<sup>2-</sup> distance hardly varies with composition. Taking into account the difference between peaks at 3.5 Å in the FTs (Figs. 5 and 6, as discussed above in Sec.

IV B), one can correlate the change in the Fe<sup>3+</sup>  $3d$  states with the variation of  $B-O-B$  bond angles and the presence of oxygen vacancies. Both effects are expected to result in  $3d$  band narrowing, and thus in more localized  $3d$  wave functions, increasing the preedge intensity for high Fe<sup>3+</sup> content (Fig. 3).

One should also note that the preedge peak intensity at the Fe  $K$  edge (Fig. 3) is slightly higher in reduced samples than in oxidized ones for the same composition. This difference can be partially attributed to a decrease of the Fe<sup>3+</sup> coordination number found in EXAFS analysis [Fig. 8 (upper panel)]. Such a phenomenon has been previously discussed for ferric complexes<sup>29</sup> and iron coordination in silicate glasses.<sup>56</sup>

The independence of the Ti<sup>4+</sup>-O<sup>2-</sup> MSDR (oxidized samples) from the iron concentration (Fig. 10) is consistent with the fact that these samples exhibit no  $x$ -dependent disorder due to oxygen vacancies and also with the observation of almost  $x$ -independent IR frequencies (Fig. 12). The finding of an almost constant Fe<sup>3+</sup>-O<sup>2-</sup> MSDR (reduced samples) over an extended concentration range from  $x \approx 0$  up to  $x = 0.75$  is not self-evident, since the concentration of oxygen vacancies which potentially induce disorder increases linearly with  $x$ . On the other hand, the Fe<sup>3+</sup>-O<sup>2-</sup> vibration frequencies observed in the IR spectra are found to be  $x$  independent. Moreover, an oxygen vacancy next to a  $B$  cation tends to displace the cation closer to the remaining oxide ions (the attractive force of the missing O<sup>2-</sup> is absent). Since Fe<sup>3+</sup> is larger than Ti<sup>4+</sup>, it is difficult for the Fe<sup>3+</sup> to approach closer to the remaining O<sup>2-</sup> anions. A tendency for the  $B$  cations to shift away from the V<sub>O</sub> was confirmed, e.g., for Fe<sub>Ti</sub>'-V<sub>O</sub> in PbTiO<sub>3</sub> by density functional theory (DFT) calculations but the displacement is significantly more pronounced for the smaller Ti<sup>4+</sup> than for the Fe<sup>3+</sup> ion.<sup>57</sup>

The variation of the Fe<sup>4+</sup>-O<sup>2-</sup> MSDR (oxidized samples) with iron concentration is nontrivial. For  $x$  close to 1, its value approaches that of the Ti<sup>4+</sup>-O<sup>2-</sup> MSDR, which seems to be reasonable since the vibrational characteristics of Fe<sup>4+</sup>-O<sup>2-</sup> and Ti<sup>4+</sup>-O<sup>2-</sup> are similar. The increase of the Fe<sup>4+</sup>-O<sup>2-</sup> MSDR with decreasing  $x$  is more astonishing. For  $x \rightarrow 0$ , it increases by a factor of about 3 and is significantly larger than the Fe<sup>3+</sup>-O<sup>2-</sup> MSDR. If one takes the MSDR of SrFeO<sub>3</sub> as a reference point for the vibrational disorder, the excess contribution is 0.006 Å<sup>2</sup> for  $x = 0$ . Since the vibrational characteristics can be assumed to be similar for all Fe<sup>4+</sup>-O<sup>2-</sup> bonds in the oxidized samples and the remaining minor oxygen vacancy concentration was shown to not increase the MSDR, this excess Fe<sup>4+</sup>-O<sup>2-</sup> MSDR contribution strongly implies a bond length distribution. In first-order approximation, the MSDR is the sum of a static and a vibrational disorder component,<sup>20</sup>

$$\text{MSDR} = \text{MSDR}_{\text{stat}} + \text{MSDR}_{\text{vib}}, \quad (3)$$

and from  $\text{MSDR}_{\text{stat}} = 0.006 \text{ \AA}^2$  ( $x = 0$ ), the bond length distribution is calculated from<sup>20</sup>

$$\Delta r = \frac{m+n}{\sqrt{mn}} \sqrt{\text{MSDR}_{\text{stat}}}, \quad (4)$$

resulting in  $\Delta r \approx 0.16 \text{ \AA}$  (here, we inserted  $m=4$  and  $n=2$  corresponding to a JT distortion, but setting  $m=n$  hardly changes the numerical result). A plausible explanation for such a distribution occurring only for  $\text{Fe}^{4+}$  and not for  $\text{Ti}^{4+}$  or  $\text{Fe}^{3+}$  could be a JT distortion. This broadening of the bond length distribution is significantly larger than the Fe-O distance increase of  $0.03 \text{ \AA}$  between  $x=1$  and  $x \rightarrow 0$ . The magnitude of the total distortion of  $0.16 \text{ \AA}$  is larger than the sum of the contraction of  $0.028 \text{ \AA}$  along the  $x, y$  axes and the elongation of  $0.052 \text{ \AA}$  along the  $z$  direction found in quantum chemical calculations of an isolated  $\text{Fe}^{4+}$  in  $\text{SrTiO}_3$ .<sup>3</sup>

Since the respective transitions are allowed in cubic perovskites, the IR peaks observed in Fig. 12 represent an average over the contributions from Ti-O and Fe-O bond vibrations. For the oxidized samples, the IR frequencies are almost independent of the iron concentration  $x$ , therefore, we expect that (independent of the exact model) the vibrational contribution to the MSRD of  $\text{Fe}^{4+}\text{-O}^{2-}$  is also independent of  $x$ . A splitting of IR peaks due to a JT distortion around  $\text{Fe}^{4+}$  would not show up in the IR spectra because for small  $x \leq 0.03$  (where the strongest JT effect is expected), their statistical weight is too small, while for large  $x$ , the JT distortion is expected to vanish.

In contrast to the IR measurements, the Raman spectra are sensitive to local symmetry reduction since the undistorted cubic perovskites exhibit no allowed first-order peaks at all. The pronounced new peak at  $690 \text{ cm}^{-1}$  appears for the oxidized samples with low to moderate iron content, while the spectra of the reduced samples remain essentially unchanged although at a first glance, the incorporation of  $\text{Fe}^{3+}$  and oxygen vacancies should induce an even stronger symmetry reduction. This could be interpreted as an indication for the local symmetry reduction being inseparably related to the  $4+$  oxidation state of iron. While such a local symmetry breaking could be caused by an anisotropic JT-type distortion or alternatively by an isotropic bond length change around  $\text{Fe}^{4+}$ , the observed broadening of the  $\text{Fe}^{4+}\text{-O}^{2-}$  distance distribution at only slightly increasing bond length (see discussion above) and the concentration dependence of this Raman line (see below) clearly favor the first interpretation. The absence of an intensity decrease (and even a peak intensity increase observed) upon cooling shows that the peak does not arise from anharmonicity effects.

For the lowest iron concentrations  $x < 0.03$ , the  $690 \text{ cm}^{-1}$  Raman peak area is approximately proportional to the Fe concentration, already for  $x \geq 0.03$ , the peak area decreases with the increase in  $x$ . Obviously a continuous decrease of the JT distortion with increasing iron concentration occurs which shows up in the decreasing excess contribution to the  $\text{Fe}^{4+}\text{-O}^{2-}$  MSRD as well as in the decreasing Raman peak area (note that these two quantities are not necessarily proportional). The decrease of the line intensity already at  $x > 0.03$  is difficult to rationalize for the symmetry breaking being caused by an isotropic local bond length change. On the other hand, the fact that in this Fe concentration range also the electronic conductivity changes drastically<sup>4</sup> points toward the importance of the electronic structure. That supports that the Raman line is related to the presence of a JT distortion. In parallel to the decrease in Raman peak area, the FWHM of the  $690 \text{ cm}^{-1}$  peak increases. A similar behavior

was observed for rhombohedral  $\text{La}_{0.93}\text{Mn}_{0.98}\text{O}_3$ ,<sup>58</sup> where a temperature decrease leads to a transition into a ferromagnetic phase with decreased deformation in the  $\text{MnO}_6$  octahedra. The intensity of the Raman peaks at  $499$  and  $517 \text{ cm}^{-1}$  assigned to local JT distortions decreases with decreasing temperature and the FWHM increases, which was interpreted by a reduced phonon lifetime related to the decreasing local distortions.

In principle, an off-center position of the  $\text{Fe}^{4+}$ , e.g., along the  $z$  axis, cannot be ruled out. Such a displacement would also remove the degeneracy of the singly occupied  $e_g$  orbitals. For  $\text{Ni}^+$  and  $\text{Cu}^{2+}$  in  $\text{SrO}$ , such a combined distortion (“pseudo-JT effect”) was observed.<sup>59,60</sup> Nevertheless, it has to be emphasized that there, the substituting cation is about  $0.2 \text{ \AA}$  smaller than the  $\text{Sr}^{2+}$  ion,<sup>60</sup> while the size difference between  $\text{Fe}^{4+}$  and  $\text{Ti}^{4+}$  amounts to only  $0.02 \text{ \AA}$ .

The fact that we do not observe a splitting of the first shell due to the JT effect around  $\text{Fe}^{4+}$  ions at low concentrations directly in EXAFS spectra or in their FTs can be attributed to the type of local distortion, resulting in several groups of strongly overlapping  $\text{Fe}^{4+}\text{-O}^{2-}$  distances. As a result, the existing JT distortion expresses itself in large increase of the first shell MSRD (Fig. 11). Such an effect was observed previously in  $\text{LaMnO}_3$  (Mn, high spin  $d^4$ , coherent JT effect, monoclinic unit cell),<sup>61</sup> where the distribution of Mn-O bond lengths ranging from  $1.91$  to  $1.97$  to  $2.15 \text{ \AA}$  was also not resolved into individual peaks (although spectra were measured to high  $k$  values of  $15 \text{ \AA}^{-1}$ ), but large MSRD values were found ( $0.0095 \text{ \AA}^2$  at  $300 \text{ K}$ , being comparable to our oxidized samples with  $x \leq 0.1$ ). Also, only an anomalous MSRD increase with temperature was observed for  $(\text{Sr}_x\text{La}_{1-x})\text{MnO}_3$  samples in the temperature range where the transition from the ferromagnetic phase (no JT effect) to the paramagnetic state (JT distortion for  $\text{Mn}^{4+}$ ) occurs.<sup>62</sup> This seems to be a comparable case to our findings. For  $\text{Sr}_{0.5}\text{La}_{1.5}\text{Li}_{0.5}\text{Fe}_{0.5}^{4+}\text{O}_4$  which crystallizes in the  $\text{K}_2\text{NiF}_4$  structure with  $\text{Fe}^{4+}$  in a tetragonally distorted octahedron, a splitting of the Fe-K absorption edge by  $\approx 3 \text{ eV}$  was observed.<sup>63,64</sup> The absence of such a splitting in our case can be understood from the fact that the difference in Fe-O distances is only  $0.16 \text{ \AA}$  compared to  $0.5 \text{ \AA}$  reported for  $\text{Sr}_{0.5}\text{La}_{1.5}\text{Li}_{0.5}\text{Fe}_{0.5}^{4+}\text{O}_4$  in Refs. 63 and 64.

## VI. SUMMARY AND CONCLUSIONS

Structural studies of  $\text{Sr}(\text{Fe}_x\text{Ti}_{1-x})\text{O}_{3-\delta}$  perovskites as a function of composition and iron oxidation state have been performed by means of XRD, Fe and Ti  $K$ -edge XAS, and vibrational (Raman and infrared) spectroscopy with the emphasis on the possible Jahn-Teller distortion around  $\text{Fe}^{4+}$  ions. The local electronic structure probed by XANES, as well as the long range order probed by XRD and the short range order reflected in EXAFS, showed a dependence on composition as well as on iron oxidation state. The variation of the preedge peak intensity in the XANES signals is attributed to the modification of the Fe(Ti)-O bond lengths and  $B\text{-O-B}$  bonding angles, resulting in a change of localization of  $3d$ -metal states and their occupation numbers  $n_d$ .

Although none of the individual observations alone gives a final proof of a JT distortion around Fe<sup>4+</sup> ions, the combination of results obtained by XAS (especially the iron concentration dependence of the Fe<sup>4+</sup>-O<sup>2-</sup> MSRD) and vibrational spectroscopies strongly supports its presence, most pronounced for  $x \approx 0.03$  and decreasing for higher iron concentrations. The decrease of the JT effect with increasing  $x$  can be understood qualitatively by the change in the electronic structure of the materials from insulator to metal. A quantitative modeling of the variation of the Fe<sup>4+</sup>-O<sup>2-</sup> MSRD and the intensities of the Raman lines remains a challenging theoretical problem. More detailed DFT calculations will be reported in a forthcoming paper.

## ACKNOWLEDGMENTS

We thank the European Synchrotron Radiation Facility (ESRF) for the beam time allocation and support during experiments. The XAS measurements were performed at the ESRF under Project No. CH-1812. We thank G. Götter for recording the diffractograms, W. Dietrich for assistance with the high oxygen pressure treatment, A. Schulz for the Raman measurements, W. König (IR spectroscopy), C. Ulrich and M. Bakr (temperature-dependent Raman measurements), and P. Adler for valuable discussions, all from MPI Stuttgart.

\*r.merkle@fkf.mpg.de

- <sup>1</sup>F. A. Kröger, *The Chemistry of Imperfect Crystals* (North-Holland, Amsterdam, 1964).
- <sup>2</sup>I. Denk, W. Münch, and J. Maier, *J. Am. Ceram. Soc.* **78**, 3265 (1995).
- <sup>3</sup>R. A. Evarestov, S. Piskunov, E. A. Kotomin, and G. Borstel, *Phys. Rev. B* **67**, 064101 (2003).
- <sup>4</sup>R. Merkle and J. Maier, *Solid State Ionics* (to be published).
- <sup>5</sup>P. Adler and S. Eriksson, *Z. Anorg. Allg. Chem.* **626**, 118 (2000).
- <sup>6</sup>H. D. Zhou and J. B. Goodenough, *J. Solid State Chem.* **177**, 1952 (2004).
- <sup>7</sup>P. Adler, A. Lebon, V. Damljanović, C. Ulrich, C. Bernhard, A. V. Boris, A. Maljuk, C. T. Lin, and B. Keimer, *Phys. Rev. B* **73**, 094451 (2006).
- <sup>8</sup>R. Moos, W. Menesklou, H.-J. Schreiner, and K. H. Härdtl, *Sens. Actuators B* **67**, 178 (2000).
- <sup>9</sup>J. B. MacChesney, R. C. Sherwood, and J. F. Potter, *J. Chem. Phys.* **43**, 1907 (1965).
- <sup>10</sup>M. Schmidt and S. J. Campbell, *J. Solid State Chem.* **156**, 292 (2001).
- <sup>11</sup>C. W. Burnham, LCLSQ, Version 8.4, least-squares refinement of crystallographic lattice parameters, Department of Earth and Planetary Sciences, Harvard University, 1991.
- <sup>12</sup>A. Boultif and D. Louer, *J. Appl. Crystallogr.* **24**, 987 (1991).
- <sup>13</sup>A. Filipponi, M. Borowski, D. T. Bowron, S. Ansell, S. D. Panfilis, A. Di Cicco, and J.-P. Itie, *Rev. Sci. Instrum.* **71**, 2422 (2000).
- <sup>14</sup>A. Kuzmin, *Physica B* **208/209**, 175 (1995).
- <sup>15</sup>A. L. Ankudinov, B. Ravel, J. J. Rehr, and S. D. Conradson, *Phys. Rev. B* **58**, 7565 (1998).
- <sup>16</sup>A. Filipponi, A. Di Cicco, and C. R. Natoli, *Phys. Rev. B* **52**, 15122 (1995).
- <sup>17</sup>N. Binsted and S. S. Hasnain, *J. Synchrotron Radiat.* **3**, 185 (1996).
- <sup>18</sup>A. Kuzmin, J. Purans, M. Benfatto, and C. R. Natoli, *Phys. Rev. B* **47**, 2480 (1993).
- <sup>19</sup>A. Kuzmin, J. Purans, G. Dalba, P. Fornasini, and F. Rocca, *J. Phys.: Condens. Matter* **8**, 9083 (1996).
- <sup>20</sup>B. K. Teo, *EXAFS: Basic Principles and Data Analysis* (Springer-Verlag, Berlin, 1986).
- <sup>21</sup>J. J. Rehr and R. C. Albers, *Rev. Mod. Phys.* **72**, 621 (2000).
- <sup>22</sup>M. G. Kim, H. S. Cho, and C. H. Yo, *J. Phys. Chem. Solids* **59**, 1369 (1998).
- <sup>23</sup>M. Abbate, G. Zampieri, J. Okamoto, A. Fujimori, S. Kawasaki, and M. Takano, *Phys. Rev. B* **65**, 165120 (2002).
- <sup>24</sup>A. E. Bocquet, A. Fujimori, T. Mizokawa, T. Saitoh, H. Namatame, S. Suga, N. Kimizuka, Y. Takeda, and M. Takano, *Phys. Rev. B* **45**, 1561 (1992).
- <sup>25</sup>R. V. Vedrinskii, V. L. Kraizman, A. A. Novakovich, P. V. Demekhin, and S. V. Urazhdin, *J. Phys.: Condens. Matter* **10**, 9561 (1998).
- <sup>26</sup>M. Fujita, H. Nakamatsu, S. Sugihara, J. Aihara, and R. Sekine, *J. Comput. Chem. Jpn.* **3**, 21 (2004).
- <sup>27</sup>T. Yamamoto, T. Mizoguchi, and I. Tanaka, *Phys. Rev. B* **71**, 245113 (2005).
- <sup>28</sup>Z. Wu, C. R. Natoli, A. Marcelli, E. Paris, F. Seifert, J. Zhang, and T. Li, *J. Synchrotron Radiat.* **8**, 215 (2001).
- <sup>29</sup>T. E. Westre, P. Kennepohl, J. G. DeWitt, B. Hedman, K. O. Hodgson, and E. I. Solomon, *J. Am. Chem. Soc.* **119**, 6297 (1997).
- <sup>30</sup>Y. Joly, D. Cabaret, H. Renevier, and C. R. Natoli, *Phys. Rev. Lett.* **82**, 2398 (1999).
- <sup>31</sup>J. Danger, P. Le Fèvre, H. Magnan, D. Chandesris, S. Bourgeois, J. Jupille, T. Eickhoff, and W. Drube, *Phys. Rev. Lett.* **88**, 243001 (2002).
- <sup>32</sup>F. de Groot, *Chem. Rev. (Washington, D.C.)* **101**, 1779 (2001).
- <sup>33</sup>J. García, J. Blasco, M. G. Proietti, and M. Benfatto, *Phys. Rev. B* **52**, 15823 (1995).
- <sup>34</sup>A. Kuzmin, N. Mironova, and J. Purans, *J. Phys.: Condens. Matter* **9**, 5277 (1997).
- <sup>35</sup>A. Kuzmin and J. Purans, *J. Phys.: Condens. Matter* **5**, 267 (1993).
- <sup>36</sup>A. Kuzmin and J. Purans, *J. Phys.: Condens. Matter* **5**, 9423 (1993).
- <sup>37</sup>B. Houser and R. Ingalls, *Phys. Rev. B* **61**, 6515 (2000).
- <sup>38</sup>R. Merkle and J. Maier, *Phys. Chem. Chem. Phys.* **5**, 2297 (2003).
- <sup>39</sup>J. Rodriguez, J. A. Pereda, M. Vallet, J. G. Calbet, and J. Tejada, *Mater. Res. Bull.* **21**, 255 (1986).
- <sup>40</sup>C. Greaves and R. A. Buker, *Mater. Res. Bull.* **21**, 823 (1986).
- <sup>41</sup>R. D. Shannon, *Acta Crystallogr., Sect. A: Cryst. Phys., Diffr., Theor. Gen. Crystallogr.* **32**, 751 (1976).
- <sup>42</sup>J. Xu, A. P. Wilkinson, and S. Pattanaik, *Chem. Mater.* **12**, 3321 (2000).

- <sup>43</sup>S. C. Tarantino, P. Ghina, C. McCammon, R. Amantea, and M. A. Carpenter, *Acta Crystallogr., Sect. B: Struct. Sci.* **61**, 250 (2005).
- <sup>44</sup>E. Seviliano, H. Meuth, and J. J. Rehr, *Phys. Rev. B* **20**, 4908 (1979).
- <sup>45</sup>G. Beni and P. M. Platzman, *Phys. Rev. B* **14**, 1514 (1976).
- <sup>46</sup>T. Trautmann and C. Falter, *J. Phys.: Condens. Matter* **16**, 5955 (2004).
- <sup>47</sup>A. Yoshiasa, K. Nakajima, K. Murai, and M. Okube, *J. Synchrotron Radiat.* **8**, 940 (2001).
- <sup>48</sup>P. A. Fleury and J. M. Worlock, *Phys. Rev.* **174**, 613 (1968).
- <sup>49</sup>W. G. Nilsen and J. G. Skinner, *J. Chem. Phys.* **48**, 2240 (1968).
- <sup>50</sup>H. Vogt and G. Neumann, *Phys. Status Solidi B* **92**, 57 (1979).
- <sup>51</sup>P. Ranson, R. Ouillon, J.-P. Pinan-Lucarre, P. Pruzan, S. K. Mishra, R. Ranjan, and D. Pandey, *J. Raman Spectrosc.* **36**, 898 (2005).
- <sup>52</sup>A. A. Sirenko, I. A. Akimov, J. R. Fox, A. M. Clark, H.-C. Li, W. Si, and X. X. Xi, *Phys. Rev. Lett.* **82**, 4500 (1999).
- <sup>53</sup>A. Tkach, P. M. Vilarinho, A. L. Kholkin, P. Pashkin, P. Samoukhina, J. Pokorny, S. Veljko, and J. Petzelt, *J. Appl. Phys.* **97**, 044104 (2005).
- <sup>54</sup>H. Zheng, I. M. Reaney, G. D. C. Csete de Györgyfalva, R. Ubc, J. Yarwood, M. P. Seabra, and V. M. Ferreira, *J. Mater. Res.* **19**, 488 (2004).
- <sup>55</sup>J. B. Goodenough and J. S. Zhou, *Struct. Bonding (Berlin)* **98**, 17 (2001).
- <sup>56</sup>F. Farges, Y. Lefrère, S. Rossano, A. Berthereau, G. Calas, and G. E. Brown, Jr., *J. Non-Cryst. Solids* **344**, 176 (2004).
- <sup>57</sup>H. Meštrić *et al.*, *Phys. Rev. B* **71**, 134109 (2005).
- <sup>58</sup>M. N. Iliev and M. V. Abrashev, *J. Raman Spectrosc.* **32**, 805 (2001).
- <sup>59</sup>V. S. Vikhnin and L. S. Sochava, *Sov. Phys. Solid State* **21**, 1193 (1979).
- <sup>60</sup>V. S. Vikhnin, L. S. Sochava, and Y. N. Tolparov, *Sov. Phys. Solid State* **21**, 1023 (1979).
- <sup>61</sup>C. H. Booth, F. Bridges, G. H. Kwei, J. M. Lawrence, A. L. Cornelius, and J. J. Neumeier, *Phys. Rev. Lett.* **80**, 853 (1998).
- <sup>62</sup>C. H. Booth, F. Bridges, G. H. Kwei, J. M. Lawrence, A. L. Cornelius, and J. J. Neumeier, *Phys. Rev. B* **57**, 10440 (1998).
- <sup>63</sup>B. Buffat, M. H. Tuilier, H. Dexpert, G. Demazeau, and P. Hagemmuller, *J. Phys. Chem. Solids* **47**, 491 (1986).
- <sup>64</sup>B. Buffat and M. H. Tuilier, *Solid State Commun.* **64**, 401 (1987).